

# Universal Quantum Suppression in Frustrated Ising Magnets across the Quasi-1D to 2D Crossover via Quantum Annealing

Kumar Ghosh<sup>1,\*</sup>

<sup>1</sup>*E.ON Digital Technology, Laatzener Str. 1, 30539 Hannover, Germany*

Quantum magnets in the  $M\text{Nb}_2\text{O}_6$  and  $\text{BaCo}_2\text{V}_2\text{O}_8$  families realise frustrated transverse-field Ising models whose competing ferromagnetic and antiferromagnetic couplings generate a sign problem provably intractable for quantum Monte Carlo at any system size, leaving their quantum phase boundaries numerically inaccessible. Using a D-Wave Advantage2 quantum annealer at  $L \leq 27$  (729 spins), we obtain the first large- $L$  critical points for this model family, measuring quantum-driven transitions at  $g_c^{\text{QPU}} \in \{0.286, 0.210, 0.156, 0.093\}$  for  $\alpha \in \{1.0, 0.7, 0.5, 0.3\}$ , where the analytically exact classical threshold is  $g_c^{\text{class}}(\alpha) = 2\alpha/3$ . The suppression ratio  $r(\alpha) = g_c^{\text{QPU}}/g_c^{\text{class}}$  exhibits a sharp two-regime structure: the three quasi-1D geometries ( $\alpha \leq 0.7$ ) are mutually consistent with a universal plateau  $\bar{r} = 0.450 \pm 0.002$  ( $\chi^2/\text{dof} = 1.10$ ,  $p = 0.33$ ), demonstrating that quantum fluctuations destroy approximately 55% of the classical FM stability window independently of coupling anisotropy, while  $r$  steps down to the 2D limit above the empirical crossover scale  $\alpha^* \approx 0.7$ . Inner Binder cumulant pairs, which converge fastest to the thermodynamic limit, resolve  $r(1.0) \approx 0.412$  and a step  $\Delta r = 0.038 \pm 0.015$  from the quasi-1D plateau. A four-point linear fit  $r(\alpha) = (0.494 \pm 0.024) - (0.063 \pm 0.034)\alpha$  summarises both regimes; its  $\alpha \rightarrow 0$  intercept recovers the exact 1D result of Pfeuty within 1.7 standard deviations, and its slope is a lower bound on the true crossover amplitude concentrated in  $\alpha \in [\alpha^*, 1]$ . Two sequential blind predictions, confirmed at  $0.2\sigma$  and  $0.7\sigma$  before each measurement, validate the crossover law. All four geometries show a direct ferromagnet-to-paramagnet transition, complete quantum ergodicity ( $f_{\text{uniq}} = 1.000$ ), and null valence-bond solid order.

## I. INTRODUCTION

Frustrated quantum magnets hold a central place in condensed-matter physics because competing interactions suppress conventional order and can stabilise exotic ground states—quantum spin liquids, valence-bond solids, and quantum paramagnets—that lie outside Landau’s symmetry-breaking paradigm [1–3]. The transverse-field Ising model (TFIM) on frustrated lattices is the simplest Hamiltonian in which these phenomena compete directly with phases driven by ferromagnetic exchange [4].

Dimensional crossover in quasi-one-dimensional magnets—the evolution of collective behaviour as weakly coupled Ising chains develop two-dimensional coherence—is a long-standing and fundamentally difficult problem. The elementary excitations of a 1D system are qualitatively different from those of its 2D counterpart, and the interchain couplings that drive the crossover generate a sign problem in quantum Monte Carlo when frustrated [5]. Inelastic neutron scattering on  $\text{CoNb}_2\text{O}_6$  has directly resolved the frustrated interchain couplings in the antiferromagnetic isosceles triangular geometry that the present model realises [6], providing the experimental foundation for the zero-temperature phase diagram of Lee, Kaul, and Balents [7], who predicted five distinct quantum phases in the FM-coupled-chain sector. Because the competing FM and AFM couplings generate a provable sign problem, the

locations of these phase boundaries and the quantitative structure of the dimensional crossover have remained numerically inaccessible at system sizes relevant for finite-size scaling, even though the isolated chain is exactly solvable [8] and the geometric constraints on AFM instability are well characterised [9].

On the triangular lattice, the antiferromagnetic Wannier model [10] is exactly solvable; adding a transverse field drives a quantum phase transition whose Kibble-Zurek dynamics have been mapped in the sign-problem-free antiferromagnetic sector [11, 12]. The *ferromagnetic* nearest-neighbour variant with  $J_1 < 0$  and antiferromagnetic next-nearest-neighbour  $J_2 > 0$  is qualitatively different. Recent QPU studies of triangular frustrated systems have examined quench dynamics and material-specific properties in models that admit classical tensor-network or Monte Carlo benchmarks [13, 14]; the present model admits neither.

The quantum Hamiltonian studied here is

$$\mathcal{H} = \Gamma \sum_i \sigma_i^x + J_1 \sum_{\langle i,j \rangle_{\text{chain}}} \sigma_i^z \sigma_j^z + J_1' \sum_{\langle i,j \rangle_{\text{inter}}} \sigma_i^z \sigma_j^z + J_2 \sum_{\langle\langle i,j \rangle\rangle} \sigma_i^z \sigma_j^z, \quad (1)$$

with  $J_1 < 0$ ,  $J_1' = \alpha J_1$ ,  $J_2 > 0$ . This model cannot be accessed by conventional quantum Monte Carlo: the competing FM and AFM couplings generate a genuine sign problem that, by the theorem of Troyer and Wiese [5], cannot be eliminated by any known basis transformation. Exact diagonalisation is confined to  $L \leq 4-5$ . The D-Wave Advantage2 quantum annealer implements Eq. (1) via minor embedding onto the Zephyr Z15 hard-

\* jb.ghosh@outlook.com

ware graph [12], providing the current route to large- $L$  numerics for this sign combination.

The anisotropy  $\alpha = J'_1/J_1 \in (0, 1]$  controls the dimensional crossover from the isotropic triangular lattice ( $\alpha = 1$ ) to weakly coupled Ising chains ( $\alpha \rightarrow 0$ ), mapping directly onto  $M\text{Nb}_2\text{O}_6$  ( $M = \text{Co}, \text{Ni}$ ) and  $\text{BaCo}_2\text{V}_2\text{O}_8$ , where  $\alpha$  is fixed by crystal structure and measured by inelastic neutron scattering [6].  $\text{NiNb}_2\text{O}_6$  has  $\alpha \approx 1$  [15];  $\text{CoNb}_2\text{O}_6$  has  $\alpha \approx 0.7$  [6, 16];  $\text{BaCo}_2\text{V}_2\text{O}_8$  has  $\alpha \approx 0.5$  [17];  $\text{FeNb}_2\text{O}_6$  has  $\alpha \approx 0.3$  [16]. Inelastic neutron scattering on  $\text{CoNb}_2\text{O}_6$  [6] established the interchain frustration ratio  $J_2/J_1 = 0.76 \pm 0.10$  by parametrising the full three-dimensional spin-flip dispersion in the quantum paramagnetic phase. As shown below, this ratio substantially exceeds  $g_c^{\text{QPU}}(0.7) = 0.210$ , placing  $\text{CoNb}_2\text{O}_6$  firmly in the quantum-disordered sector and providing independent microscopic validation of the QPU phase boundary from a completely orthogonal experimental technique.

This Letter reports three principal findings. **(i)** The analytically exact classical instability threshold  $g_c^{\text{class}}(\alpha) = 2\alpha/3$  follows from the triangular lattice geometry alone. **(ii)** QPU measurements at  $\alpha \in \{0.3, 0.5, 0.7, 1.0\}$  reveal a clear two-regime structure: a universal plateau  $\bar{r} = 0.450 \pm 0.002$  ( $\chi^2/\text{dof} = 1.10$ ) spanning the entire quasi-1D sector ( $\alpha \leq \alpha^* \approx 0.7$ ), followed by a step to the 2D limit. The linear fit

$$r(\alpha) = (0.494 \pm 0.024) - (0.063 \pm 0.034) \alpha \quad (1.9\sigma) \quad (2)$$

summarises both regimes compactly; its  $\alpha \rightarrow 0$  intercept recovers the exact 1D TFIM result of Pfeuty [8] within 1.7 standard deviations. **(iii)** All four geometries show a direct FM-to-paramagnet transition with no intermediate phase, complete ergodicity bypass, and null VBS order. The combined formula  $g_c^{\text{QPU}}(\alpha) = r(\alpha) \cdot 2\alpha/3$  constitutes the first quantitative characterisation of the quantum dimensional crossover in the FM-frustrated columbite sector; prior theoretical work [7] was limited to perturbative approximations that could not access phase boundaries at FSS-relevant system sizes. Two sequential blind predictions were confirmed at 0.2 and 0.7 standard deviations, each before the respective data were acquired.

## II. MODEL AND EXPERIMENTAL DESIGN

### D-Wave implementation

The Advantage2.system1.13 processor implements

$$H(s) = -A(s) \sum_i \sigma_i^x + B(s) \left[ \sum_{i<j} J_{ij} \sigma_i^z \sigma_j^z \right], \quad (3)$$

where  $s = t/t_a \in [0, 1]$  and  $A(s)$ ,  $B(s)$  are the publicly available hardware annealing schedules [12]. The ratio  $\Gamma_{\text{eff}}(t_a) \equiv A(s_f)/B(s_f)$  evaluated at the Kibble-Zurek

freeze-out point  $s_f(t_a)$  provides the effective transverse field for each anneal time and labels the horizontal axis of the  $(g, \Gamma_{\text{eff}})$  phase diagrams.

The triangular lattice in parallelogram embedding has three nearest-neighbour bond directions,  $(+1, -1)$ ,  $(0, +1)$ , and  $(+1, 0)$ , and three next-nearest-neighbour directions,  $(0, +2)$ ,  $(+2, 0)$ , and  $(+1, +1)$ . For  $\alpha < 1$ , the bond direction  $(+1, -1)$  carries the intrachain coupling  $J_1$  while  $(0, +1)$  and  $(+1, 0)$  carry the interchain coupling  $\alpha J_1$ ; at  $\alpha = 1$  all three nearest-neighbour directions are equivalent and the model reduces to the isotropic triangular lattice. The isosceles triangular lattice is embedded onto the Zephyr Z15 hardware graph via minor embedding computed with `minorminer` [18]; the graph topology is  $\alpha$ -independent, so the same embedding is reused across all four geometries and all system sizes  $L$ . The chain-break fraction is zero across all 5,572,000 shots in the combined dataset: every physical qubit chain collapses to a single logical value on every anneal, and no logical errors enter the observables. In minor-embedded studies where chain breaks occur, residual errors broaden Binder cumulant crossings and bias the extracted  $g_c^{\text{QPU}}$  [19]; the zero chain-break fraction here eliminates this source of systematic error entirely.

The working processor has 4,579 active qubits, an extended  $J$ -range of  $[-2.0, 1.0]$ , and supports fast anneals down to  $t_a = 0.005 \mu\text{s}$ . We encode Eq. (1) by setting  $J_{ij} = J_1 = -1$  for the chain direction  $(+1, -1)$ ,  $J_{ij} = \alpha J_1$  for the two interchain directions, and  $J_{ij} = g|J_1|$  for the three NNN directions; `auto_scale=False` ensures the hardware applies the programmed values without rescaling. The processor operates at  $T_{\text{proc}} \approx 15 \text{ mK}$ , giving  $T_{\text{proc}}/|J_1| \lesssim 10^{-2}$ , placing every  $(g, t_a)$  point firmly in the quantum regime.

### Parameter grids

For  $\alpha = 1$  we use  $L \in \{9, 12, 15, 18, 21, 24, 27\}$ , 14 frustration values dense near the transition, and 14 annealing times  $t_a \in [5 \text{ ns}, 500 \mu\text{s}]$ , giving 1,372,000 shots. For each of  $\alpha \in \{0.5, 0.7\}$  we use  $L \in \{15, 18, 21, 24, 27\}$  with 20-point frustration grids ( $\delta g = 0.002$  in the critical window), giving 1,400,000 shots per geometry; for  $\alpha = 0.5$  the grid extends to  $g = 0.40$ , placing both  $g_c^{\text{QPU}}$  and  $g_c^{\text{class}} = 1/3$  within the scan range. For  $\alpha = 0.3$  we use  $L \in \{15, 18, 21, 24, 27\}$  with a 20-point grid over  $g \in [0, 0.30]$ , giving 1,400,000 shots; both  $g_c^{\text{QPU}} \approx 0.093$  and  $g_c^{\text{class}} = 0.200$  lie within this range. Annealing times span fast anneals ( $t_a \leq 0.5 \mu\text{s}$ , `fast_anneal=True`) and slow anneals ( $t_a \geq 1 \mu\text{s}$ ), with  $N_{\text{reads}} = 1,000$  per  $(g, t_a, L)$  point.

### Observables and effective temperature calibration

Raw spin configurations  $\{s_i^{(k)}\}_{k=1}^{N_{\text{reads}}}$  are read back at each  $(g, t_a, L)$  point. The *three-sublattice Binder cumu-*

lant

$$U_{4,\sqrt{3}} = 1 - \frac{\langle \psi_{\sqrt{3}}^4 \rangle}{3 \langle \psi_{\sqrt{3}}^2 \rangle^2},$$

$$\psi_{\sqrt{3}} = |m_A + \omega m_B + \omega^2 m_C|, \quad \omega = e^{2\pi i/3}, \quad (4)$$

is the primary FSS observable; curves for different  $L$  cross at  $g_c$ . We also compute the total-magnetisation Binder cumulant  $U_4$ , sublattice magnetisations ( $m_A, m_B, m_C$ ), the  $\sqrt{3} \times \sqrt{3}$  structure factor  $S_{\sqrt{3}}$ , FM susceptibility  $\chi_{\text{FM}}$ , plaquette order  $\mathcal{O}_{\text{plaq}}$ , string VBS order  $\mathcal{O}_{\text{VBS}}$ , and degeneracy fraction  $f_{\text{uniq}} = N_{\text{unique}}/N_{\text{reads}}$ .

For slow anneals ( $t_a \geq 1 \mu\text{s}$ ), an effective inverse temperature  $\beta_{\text{eff}}$  is calibrated by maximising the pseudolikelihood

$$\text{PLL}(\beta) = \sum_{i,k} [\beta s_i^{(k)} (\mathbf{J}\mathbf{s}^{(k)})_i + \ln \cosh(\beta |(\mathbf{J}\mathbf{s}^{(k)})_i|)] \quad (5)$$

over  $\beta \in [0.001, 50]$ , converting raw susceptibility  $\chi_{\text{raw}} = N(\langle m^2 \rangle - \langle |m| \rangle^2)$  and specific heat  $C_{V,\text{raw}} = \text{Var}(E)/N$  to physical units via  $\chi = \beta_{\text{eff}} \chi_{\text{raw}}$  and  $C_V = \beta_{\text{eff}}^2 C_{V,\text{raw}}$ . Fast anneals ( $t_a \leq 0.5 \mu\text{s}$ ) are used exclusively to characterise ergodicity bypass through  $f_{\text{uniq}}$ .

### III. RESULTS

#### 1. Analytical classical instability: $g_c^{\text{class}}(\alpha) = 2\alpha/3$

The exchange Fourier transform at the zone-boundary  $K$ -point  $\mathbf{k}_* = (2\pi/3, 2\pi/3)$  gives

$$J(\mathbf{k}_*) - J(\mathbf{0}) = 6\alpha - 9g, \quad (6)$$

where the chain structure factor  $S_{\text{chain}}(\mathbf{k}_*) = 2 \cos(\pi/3) + 2 \cos(-\pi/3) = 2$ , the interchain structure factor  $S_{\text{inter}}(\mathbf{k}_*) = 2 \cos(2\pi/3) + 2 \cos(-2\pi/3) = -2$ , and the three NNN cosines at  $\mathbf{k}_*$  each equal  $-1/2$ , giving  $S_{\text{NNN}}(\mathbf{k}_*) = -3$ , so that  $J(\mathbf{k}_*) - J(\mathbf{0}) = |J_1|(2\alpha \cdot (-2)/2 + g \cdot (-3) \cdot (-1)) = 6\alpha - 9g$  in units of  $|J_1|$ . Setting Eq. (6) to zero gives the exact classical instability threshold

$$g_c^{\text{class}}(\alpha) = \frac{2\alpha}{3} \quad (7)$$

with no free parameters. For  $g < g_c^{\text{class}}(\alpha)$ ,  $J(\mathbf{k}) - J(\mathbf{0}) > 0$  for all  $\mathbf{k} \neq \mathbf{0}$ , so the FM ground state is classically stable throughout the quantum-critical window. The geometric origin of this threshold—that each NNN bond shares two common NN bonds per site, tying the AFM instability directly to the FM backbone—was analysed by Villain et al. [9] and further developed by Moessner, Sondhi, and Chandra [20]. The threshold is confirmed numerically for all four  $\alpha$  values (Fig. 1).

#### 2. Dimensional crossover in the quantum suppression ratio

The QPU measurements establish

$$\begin{aligned} g_c^{\text{QPU}}(1.0) &= 0.286 \pm 0.012, \\ g_c^{\text{QPU}}(0.7) &= 0.210 \pm 0.001, \\ g_c^{\text{QPU}}(0.5) &= 0.156 \pm 0.004, \\ g_c^{\text{QPU}}(0.3) &= 0.093 \pm 0.005. \end{aligned} \quad (8)$$

In all four cases  $g_c^{\text{QPU}} \ll g_c^{\text{class}}(\alpha)$  (Figs. 1, 2 and Table I): the FM ground state is classically stable at each measured  $g_c^{\text{QPU}}$ , confirming that all four transitions are quantum-driven. These are the first large- $L$  determinations of any critical point in this sign-problem model family.

*a. Two-regime structure and crossover scale.* The dimensionless ratio  $r(\alpha) = g_c^{\text{QPU}}(\alpha)/g_c^{\text{class}}(\alpha)$  isolates the effect of quantum fluctuations by factoring out the trivial  $\alpha$ -dependence of the classical critical scale. The suppression ratios  $r(0.3) = 0.463$ ,  $r(0.5) = 0.467$ ,  $r(0.7) = 0.450$ , and  $r(1.0) = 0.428$  reveal a clear two-regime structure (Fig. 2). The three quasi-1D geometries  $\alpha \in \{0.3, 0.5, 0.7\}$  are mutually consistent with a universal plateau  $\bar{r} = 0.450 \pm 0.002$  ( $\chi^2/\text{dof} = 1.10$ ,  $p = 0.33$ ): quantum fluctuations destroy approximately 55% of the classical FM stability window *independently of coupling anisotropy*, confirmed across three geometries spanning  $\text{FeNb}_2\text{O}_6$ ,  $\text{BaCo}_2\text{V}_2\text{O}_8$ , and  $\text{NiNb}_2\text{O}_6$ . The  $\alpha$  values span a factor of more than two (0.3 to 0.7) in coupling ratio; the  $\chi^2/\text{dof} = 1.10$  confirms that the plateau is genuine, not a trivial consequence of approximate quasi-1D character.

At  $\alpha > \alpha^* \approx 0.7$ ,  $r$  steps down as the system crosses over toward the 2D isotropic limit. The inner Binder cumulant pairs (18, 21) and (21, 24), which converge fastest to the thermodynamic limit, consistently give  $g_c^{\text{QPU}}(1.0) \approx 0.275$  and  $r(1.0) \approx 0.412$ , a separation  $\Delta r = 0.038 \pm 0.015$  from the quasi-1D plateau ( $2.5\sigma$ ). The conservative weighted mean  $g_c^{\text{QPU}}(1.0) = 0.286 \pm 0.012$ —which includes the non-monotonically drifting outer (24, 27) pair, a well-known finite-size artefact of the isotropic 2D geometry where larger effective coordination amplifies Binder non-monotonicity—gives  $r(1.0) = 0.428$  and  $\Delta r = 0.022 \pm 0.018$  ( $1.2\sigma$ ); we report this conservative value while noting that the inner-pair estimate is the better approximation to the thermodynamic critical point. The two-regime structure directly identifies  $\alpha^* \approx 0.7$  as the empirical crossover scale: below it, the 1D Pfeuty fixed point controls quantum suppression; above it, growing interchain coordination stiffens the FM backbone and drives  $r$  downward toward the 2D fixed point.

The four-point linear fit in Eq. (2) provides a compact algebraic summary of both regimes with slope significance  $1.9\sigma$ . Its  $\alpha \rightarrow 0$  intercept  $r_0 = 0.494 \pm 0.024$  recovers the exact 1D TFIM result  $r^{\text{1D}} = \Gamma_c/|J_1| = 1/2$  of

Pfeuty [8] within 1.7 standard deviations—a non-trivial check since the Pfeuty chain carries neither NNN frustration nor interchain coupling. The plateau value  $\bar{r} = 0.450$  lies below  $r^{1D} = 0.500$ : even weak interchain coupling ( $\alpha \leq 0.7$ ) reduces  $r$  below its pure-chain limit, yet the  $\alpha \rightarrow 0$  extrapolation recovers it, confirming the plateau is anchored by the 1D fixed point.

The linear fit slope is a lower bound on the true crossover amplitude for two reinforcing reasons. Physically,  $r(\alpha)$  is a nonlinear crossover function interpolating between the 1D Pfeuty fixed point ( $r \rightarrow 1/2$  as  $\alpha \rightarrow 0$ ) and the equilateral 2D triangular fixed point at  $\alpha > 1$ ; the variation is concentrated in the narrow window  $\alpha \in [\alpha^*, 1] \approx [0.7, 1.0]$ , so a linear fit distributed over the full range underestimates the true steepness. Additionally, the physical  $\alpha = 1$  geometry retains a measurable isosceles distortion ( $t_2/t_1 = 0.82 \pm 0.01$  [6]): the truly equilateral 2D fixed point lies at  $\alpha > 1$ , making the observed step  $\Delta r \approx 0.038$  itself a lower bound on the full quasi-1D to 2D crossover amplitude. Definitively resolving  $\alpha^*$  and the step amplitude requires  $L \geq 45$ .

Combining Eqs. (7) and (2):

$$g_c^{\text{QPU}}(\alpha) = r(\alpha) \cdot \frac{2\alpha}{3} = \frac{\alpha}{3}(0.988 - 0.126\alpha). \quad (9)$$

This reproduces all four measured values to within  $\pm 0.012$ .

Figure 2 (right) shows the quantum-only windows  $\Delta g(\alpha) = g_c^{\text{class}}(\alpha) - g_c^{\text{QPU}}(\alpha)$ ; the ratio  $\Delta g/g_c^{\text{class}} = 1 - r(\alpha)$  increases from  $\approx 0.57$  at  $\alpha = 1$  toward  $\approx 0.55$  for  $\alpha \leq 0.7$ , directly visualising the crossover. For  $\alpha \leq 0.5$ , both thresholds fall within the scan range, producing a double-minimum structure in the Binder cumulant that cleanly separates the quantum-driven transition from the classical instability (Fig. 3, bottom rows). Its observation at two independent geometries ( $\alpha = 0.5$  and  $\alpha = 0.3$ ) with distinct material realisations establishes it as a universal signature of the frustrated FM-AFM TFIM in the quasi-1D regime.

*b. Blind predictions.* The four geometries were measured sequentially:  $\alpha = 1.0, 0.7, 0.5$ , then  $0.3$ . *First:* the two-point fit to  $\alpha \in \{0.7, 1.0\}$  predicted  $g_c^{\text{QPUpred}}(0.5) = 0.155 \pm 0.004$ , confirmed at  $g_c^{\text{QPU}}(0.5) = 0.156 \pm 0.004$  ( $0.2\sigma$ ). *Second:* the three-point fit to  $\alpha \in \{0.5, 0.7, 1.0\}$  predicted  $g_c^{\text{QPUpred}}(0.3) = 0.096 \pm 0.003$ , confirmed at  $g_c^{\text{QPU}}(0.3) = 0.093 \pm 0.005$  ( $0.7\sigma$ ). Two successive sub- $1\sigma$  confirmations from sequentially richer fits provide strong evidence that Eq. (9) captures genuine dimensional-crossover physics rather than an artefact of the specific  $\alpha$  values studied.

*c. Physical interpretation.* Each site in the isosceles model carries 2 chain bonds (coupling  $J_1$ ) and 4 interchain bonds (coupling  $\alpha J_1$ ). As  $\alpha$  increases from 0 to 1, each additional interchain bond reinforces the FM backbone, making it progressively harder for the transverse field to disorder the system and reducing  $r$ . The pinning of  $r$  at  $\bar{r} = 0.450$  for all  $\alpha \leq \alpha^*$  reflects a

threshold: once interchain coupling falls below  $\alpha^* \approx 0.7$ , the quasi-1D fixed point dominates quantum suppression and further reduction of  $\alpha$  produces no measurable change. The crossover to 2D behaviour is concentrated in  $\alpha \in [0.7, 1.0]$ , where rapidly growing effective coordination stiffens the FM backbone and drives  $r$  downward.

### 3. Critical point determinations

For each  $\alpha$ ,  $g_c^{\text{QPU}}$  is determined at  $t_a = 500 \mu\text{s}$  by three independent methods: (a) pairwise Binder cumulant crossings ( $U_{4,\sqrt{3}}$  for  $\alpha \geq 0.5$ ;  $U_4$  for  $\alpha = 0.3$ , where  $U_{4,\sqrt{3}}$  diverges strongly in the FM phase at small  $L$ ), (b) Binder cumulant vs  $1/L$  finite-size extrapolation, and (c)  $\chi_{\text{FM}}$  peak-position extrapolation. All three agree within  $\pm 0.006$  for  $\alpha \geq 0.5$  and  $\pm 0.008$  for  $\alpha = 0.3$  (Fig. 3). Figure 4 shows that  $g_c^{\text{QPU}}(t_a)$  converges to a  $t_a$ -independent value for  $t_a \gtrsim 20 \mu\text{s}$  across all four geometries, confirming that the critical points are intrinsic properties of the model Hamiltonian and not artefacts of the annealing protocol.

*d.  $\alpha = 1.0$ .* All pairwise Binder cumulant crossings from  $L \in \{15, 18, 21, 24, 27\}$  give weighted mean  $0.286 \pm 0.012$ ; inner pairs (18, 21) and (21, 24) both cross at  $g \approx 0.275$  while the outer (24, 27) pair crosses at 0.300, reflecting non-monotonic finite-size drift at the isotropic 2D geometry. We report  $g_c^{\text{QPU}}(1.0) = 0.286 \pm 0.012$ , with the inner-pair value  $g \approx 0.275$  as the best estimate of the thermodynamic critical point.

*e.  $\alpha = 0.7$  ( $\text{CoNb}_2\text{O}_6$ ).* Inner pairs (18, 21), (21, 24), and (24, 27) give crossings 0.212, 0.209, and 0.210, spanning  $\delta g_c = 0.003$ ; bootstrap weighted mean  $0.210 \pm 0.001$ .

*f.  $\alpha = 0.5$  ( $\text{BaCo}_2\text{V}_2\text{O}_8$ ).* Inner-pair crossing at 0.156;  $U_{4,\sqrt{3}}-1/L$  sign change between  $g = 0.154$  and 0.158;  $\chi_{\text{FM}}$ -peak extrapolation 0.152–0.158. We report  $g_c^{\text{QPU}}(0.5) = 0.156 \pm 0.004$ , confirming the blind prediction  $0.155 \pm 0.004$  within  $0.2\sigma$ .

*g.  $\alpha = 0.3$  ( $\text{FeNb}_2\text{O}_6$ ).* At this geometry  $U_{4,\sqrt{3}}$  diverges strongly in the FM phase for small  $L$ , so the total FM Binder cumulant  $U_4$  serves as the primary crossing observable; at  $g \approx 0.093$  the  $U_{4,\sqrt{3}}$  and  $U_4$  crossings agree within  $\pm 0.005$ , confirming the switch does not bias the extracted critical point. Pairwise  $U_4$  crossings give weighted mean  $0.093 \pm 0.005$ ;  $\chi_{\text{FM}}$ -peak extrapolation gives 0.095–0.098. Both thresholds  $g_c^{\text{QPU}} \approx 0.093$  and  $g_c^{\text{class}} = 0.200$  lie within the scan range, producing the same double-minimum Binder structure as  $\alpha = 0.5$ . We report  $g_c^{\text{QPU}}(0.3) = 0.093 \pm 0.005$ , confirming the blind prediction  $0.096 \pm 0.003$  within  $0.7\sigma$ .

### 4. Direct FM→paramagnet transition across all $\alpha$

For all four values of  $\alpha$ ,  $m_A$ ,  $m_B$ , and  $m_C$  drop simultaneously to zero at  $g_c^{\text{QPU}}(\alpha)$  with no relative sublattice splitting at any  $g$  or  $t_a$  (Fig. 5). The  $\sqrt{3} \times \sqrt{3}$

TABLE I. Summary of quantum and classical critical points.  $g_c^{\text{class}}(\alpha) = 2\alpha/3$  is analytically exact.  $r = g_c^{\text{QPU}}/g_c^{\text{class}}$ ,  $\delta r = \delta g_c^{\text{QPU}}/g_c^{\text{class}}$ ;  $r_{\text{fit}}$  from Eq. (2);  $\Delta g = g_c^{\text{class}} - g_c^{\text{QPU}}$ . Parenthetical uncertainties on  $g_c^{\text{QPU}}$  are in the last digit.

$\alpha$	Material	$g_c^{\text{class}}$	$g_c^{\text{QPU}}$	$r \pm \delta r$	$r_{\text{fit}}$	$\Delta g$
1.0	Isotropic	0.667	0.286(12)	$0.428 \pm 0.018$	0.431	0.381
0.7	NiNb <sub>2</sub> O <sub>6</sub>	0.467	0.210(1)	$0.450 \pm 0.002$	0.450	0.257
0.5	BaCo <sub>2</sub> V <sub>2</sub> O <sub>8</sub>	0.333	0.156(4)	$0.467 \pm 0.012$	0.462	0.177
0.3	FeNb <sub>2</sub> O <sub>6</sub>	0.200	0.093(5)	$0.463 \pm 0.025$	0.475	0.107

structure factor  $S_{\sqrt{3}}/L^2$  shows no  $L$ -growth above  $g_c^{\text{QPU}}$ , ruling out any intermediate ordered phase. Energy histograms at  $t_a = 500 \mu\text{s}$  are unimodal at all  $g$  near  $g_c^{\text{QPU}}$  across  $L \in \{18, 21, 24, 27\}$  for all four geometries, consistent with continuous transitions.

The mechanism is  $\alpha$ -independent: on the triangular lattice, each NNN bond shares two common NN bonds per site [9, 20], so partial AFM NNN ordering necessarily disrupts FM NN exchange simultaneously, incurring a large energy penalty. This geometric constraint, rather than any specific coupling ratio, enforces the direct transition for all  $\alpha \in [0.3, 1]$ . The theoretical phase diagram of Lee et al. [7] argued for direct transitions in the FM-dominated sector on perturbative grounds; the present QPU measurements confirm this numerically at system sizes far beyond the reach of those methods. The field-induced  $\sqrt{3} \times \sqrt{3}$ -type spin-flip phases observed in CoNb<sub>2</sub>O<sub>6</sub> [6] require an applied field for stabilisation and are absent at zero field, fully consistent with the null  $\sqrt{3} \times \sqrt{3}$  order found here. The absence of incommensurate structure-factor growth confirms the QPU measurements remain within the FM-dominated sector, well below the IC phase boundary whose onset wavevector  $q_x^* = 2 \cos^{-1}(-\alpha/2)$  shifts with  $\alpha$  [7].

### 5. Quantum ergodicity bypass and null VBS

At  $t_a = 5 \text{ ns}$ ,  $f_{\text{uniq}} = 1.000$  for all  $L$  and all four  $\alpha$  values (Fig. 6): every anneal produces a distinct spin configuration, demonstrating quantum tunnelling through the exponentially large configuration space near each critical point. These energy barriers have a direct experimental counterpart: Heid et al. [16] report anomalously long relaxation times for all field-induced transitions in CoNb<sub>2</sub>O<sub>6</sub> at low temperatures, attributed to the energy cost of reversing entire ferromagnetic chains—the same barriers the QPU bypasses via quantum tunnelling at  $t_a = 5 \text{ ns}$ . At  $g \approx g_c^{\text{QPU}}(\alpha)$ ,  $f_{\text{uniq}} > 0.5$  persists until  $t_a \approx 5 \mu\text{s}$ , decaying more slowly than the FM anchor ( $g = 0$ , frozen by  $t_a \approx 1 \mu\text{s}$ ), consistent with enhanced degeneracy at each quantum critical point. This behaviour is identical across all four geometries, confirming ergodicity bypass is a property of the quantum fluctuations and the frustrated critical point, not of any specific  $\alpha$ . Plaquette order  $\mathcal{O}_{\text{plaq}}$  and string VBS order  $\mathcal{O}_{\text{VBS}}$  ex-

trapolate to zero as  $L \rightarrow \infty$  at all accessible  $t_a$  [20].

## IV. DISCUSSION

*a. Accessing a sign-problem model.* The model in Eq. (1) cannot be simulated by quantum Monte Carlo at any system size [5]; exact diagonalisation reaches at most  $L = 5$ . Prior QPU experiments on frustrated magnets operated exclusively in the sign-problem-free antiferromagnetic sector, where classical algorithms provide independent benchmarks [11–14]. The present work occupies a fundamentally different regime: there is no classical method to compare against, and the QPU results constitute the first large- $L$  numerical data for this model family. The plateau  $\bar{r} = 0.450 \pm 0.002$ , confirmed independently across three materials spanning a factor of more than two in coupling ratio, is a genuinely new physical result—a universal ratio that no perturbative or classical method could have predicted—complementing the perturbative phase diagram of Lee et al. [7] with the first quantitative phase boundaries at FSS-relevant system sizes.

*b. Measurement validity.* Three mutually independent lines of evidence validate the QPU results in the absence of a classical benchmark. First, the zero chain-break fraction across all 5,572,000 shots provides an empirical guarantee of embedding fidelity: every logical spin is unambiguously defined on every anneal, with no residual broadening of Binder crossings. Second, the  $t_a$ -independence of  $g_c^{\text{QPU}}$  for  $t_a \gtrsim 20 \mu\text{s}$  (Fig. 4) confirms the critical points are intrinsic to the model Hamiltonian. Third, two successive sub- $1\sigma$  blind predictions and the independent neutron-scattering corroboration of the CoNb<sub>2</sub>O<sub>6</sub> phase boundary together establish the QPU as a quantitatively reliable analogue computer for this class of sign-problem models.

*c. Predictive power and experimental roadmap.* Equation (9) provides the quantum phase boundary for any member of the MNb<sub>2</sub>O<sub>6</sub> and BaCo<sub>2</sub>V<sub>2</sub>O<sub>8</sub> families with a known structural anisotropy, without further QPU measurements. For CoNb<sub>2</sub>O<sub>6</sub> ( $\alpha \approx 1$ ), inelastic neutron scattering yields the dominant intrachain FM exchange  $J_z = 2.19 \text{ meV}$  from spin-wave parametrisation of the full three-dimensional dispersion [6] (a lower bound due to quantum renormalisation of the dispersion bandwidth). Our measurement  $g_c^{\text{QPU}}(1.0) = 0.286 \pm 0.012$  then predicts the NNN frustration at the quantum critical point as  $J_{2c} = 0.286 J_z \approx 0.63 \text{ meV}$ , independently corroborated by  $J_2/J_1 = 0.76 \pm 0.10$  from the full spin-flip dispersion [6], which substantially exceeds  $g_c^{\text{QPU}}(1.0) = 0.286$  and confirms CoNb<sub>2</sub>O<sub>6</sub> sits firmly in the quantum-disordered sector. For FeNb<sub>2</sub>O<sub>6</sub> ( $\alpha \approx 0.3$ ), the reduced interchain coupling places the material frustration ratio potentially close to  $g_c^{\text{QPU}}(0.3) = 0.093$ , making it the columbite family member closest to the quantum phase boundary and the most promising target for polarised neutron diffraction seeking simultaneous vanishing of all three sublattice magnetisations with no onset of  $\sqrt{3} \times \sqrt{3}$

order. For  $\text{BaCo}_2\text{V}_2\text{O}_8$ , the predicted critical field in the frustrated FM sector is distinct from the field-induced incommensurate ordering [17] and the one-dimensional critical field [21], which both occur in the antiferromagnetic intrachain sector under a longitudinal field; the present transition operates in a coupling regime orthogonal to those studies.

*d. Broader context.* The strategy of using a QPU with minor embedding to extract quantitative critical properties from a provably QMC-intractable model is not specific to the frustrated Ising geometry. A related demonstration for the Sherrington-Kirkpatrick spin glass at up to  $N = 4000$  spins is given in Ref. [22]. Whether analogous approaches extend to models with itinerant degrees of freedom depends on future advances in hardware connectivity; the present study establishes the strategy's feasibility in the spin-model sector.

*e. Finite-size corrections and open questions.* Non-monotonic Binder drift is most pronounced at  $\alpha = 1.0$  (pairwise spread  $\delta g_c = 0.025$ , weighted uncertainty  $\pm 0.012$ ) and smallest at  $\alpha = 0.7$  (inner-pair spread  $\delta g_c = 0.003$ ), reflecting the stronger finite-size effects of the isotropic 2D geometry. The present  $L \leq 27$  exhausts the qubit budget of the Advantage2 processor for this embedding. Three open questions require  $L \geq 45$ : (i) the universality class ( $\nu \approx 0.40\text{--}0.51$  across all four geometries, consistently below  $\nu_{3\text{D Ising}} = 0.630$ , suggesting a non-standard class but inconclusive at current sizes); (ii) the order of the transitions (energy histograms are unimodal at all present sizes, consistent with continuous transitions, but the Lee-Kosterlitz diagnostic is inconclusive); and (iii) the precise crossover scale  $\alpha^*$  and step amplitude  $\Delta r$ .

## V. CONCLUSION

We have presented the first systematic large-scale numerical study of the frustrated FM-AFM transverse-

field  $J_1$ - $J_2$  Ising model on the isosceles triangular lattice, using a D-Wave Advantage2 QPU at  $L \leq 27$  across  $\alpha \in \{0.3, 0.5, 0.7, 1.0\}$ . Because the model has a provable sign problem, these are also the first phase boundaries for this family at any FSS-relevant system size.

The central result is a two-regime dimensional crossover in the quantum suppression ratio. Three independent quasi-1D geometries ( $\text{FeNb}_2\text{O}_6$ ,  $\text{BaCo}_2\text{V}_2\text{O}_8$ ,  $\text{NiNb}_2\text{O}_6$ ) are mutually consistent with a universal plateau  $\bar{r} = 0.450 \pm 0.002$  ( $\chi^2/\text{dof} = 1.10$ ), demonstrating that quantum fluctuations destroy approximately 55% of the classical FM stability window throughout the quasi-1D sector irrespective of coupling anisotropy, with the plateau anchored by the 1D Pfeuty fixed point ( $r_0 = 0.494 \pm 0.024$ , consistent with  $r^{1\text{D}} = 1/2$  within  $1.7\sigma$ ). At  $\alpha > \alpha^* \approx 0.7$  the system crosses over to 2D behaviour; inner Binder cumulant pairs resolve a step  $\Delta r = 0.038 \pm 0.015$  ( $2.5\sigma$ ). The linear fit  $r(\alpha) = 0.494 - 0.063\alpha$  ( $1.9\sigma$ ) summarises both regimes; its slope is a lower bound on the true crossover amplitude, which is concentrated in  $\alpha \in [\alpha^*, 1]$ , is inherently nonlinear, and is further suppressed by the residual isosceles distortion ( $t_2/t_1 = 0.82$  [6]) of the physical  $\alpha = 1$  geometry. Two sequential blind predictions confirmed at  $0.2\sigma$  and  $0.7\sigma$ , together with independent neutron-scattering validation for  $\text{CoNb}_2\text{O}_6$ , establish the QPU as a reliable analogue computer for this class of sign-problem models.

Equation (9) now provides a predicted quantum phase boundary for any member of the  $\text{MNb}_2\text{O}_6$  or  $\text{BaCo}_2\text{V}_2\text{O}_8$  families with a known structural anisotropy, supplying concrete quantitative targets for neutron scattering experiments. Open questions—universality class, transition order, and the precise crossover scale  $\alpha^*$ —await  $L \geq 45$  hardware.

- 
- [1] L. Balents, *Nature* **464**, 199 (2010).
  - [2] L. Savary and L. Balents, *Rep. Prog. Phys.* **80**, 016502 (2017).
  - [3] H. T. Diep, ed., *Frustrated Spin Systems* (World Scientific, Singapore, 2005).
  - [4] S. Sachdev, *Quantum Phase Transitions*, 2nd ed. (Cambridge University Press, Cambridge, 2011).
  - [5] M. Troyer and U.-J. Wiese, *Phys. Rev. Lett.* **94**, 170201 (2005).
  - [6] I. Cabrera, J. D. Thompson, R. Coldea, D. Prabhakaran, R. I. Bewley, T. Guidi, J. A. Rodriguez-Rivera, and C. Stock, *Phys. Rev. B* **90**, 014418 (2014).
  - [7] S.-H. Lee, R. K. Kaul, and L. Balents, *Nat. Phys.* **6**, 702 (2010).
  - [8] P. Pfeuty, *Ann. Phys.* **57**, 79 (1970).
  - [9] J. Villain, R. Bidaux, J.-P. Carton, and R. Conte, *J. Phys. (Paris)* **41**, 1263 (1980).
  - [10] G. H. Wannier, *Phys. Rev.* **79**, 357 (1950).
  - [11] A. D. King, S. Suzuki, J. Raymond, A. Zucca, T. Lanting, F. Altomare, A. J. Berkley, S. Eichhorn, E. Hoskinson, M. W. Johnson, *et al.*, *Nat. Phys.* **18**, 1324 (2022).
  - [12] A. D. King *et al.*, *Science* **388**, 199 (2025).
  - [13] A. Ali *et al.*, *Nat. Commun.* **15**, 10756 (2024).
  - [14] H. Park and H. Lee, *Journal of the Physical Society of Japan* **91**, 074001 (2022).
  - [15] R. Coldea, D. A. Tennant, E. M. Wheeler, E. Wawrzynska, D. Prabhakaran, M. Telling, K. Habicht, P. Smeibidl, and K. Kiefer, *Science* **327**, 177 (2010).
  - [16] C. Heid, H. Weitzel, P. Burlet, M. Bonnet, W. Gonschorek, T. Vogt, J. Norwig, and H. Fuess, *Journal of Magnetism and Magnetic Materials* **151**, 123 (1995).
  - [17] S. Kimura, M. Matsuda, T. Masuda, S. Hondo, K. Kaneko, N. Metoki, M. Hagiwara, T. Takeuchi, K. Okumishi, Z. He, K. C. Yi, Y. Yoshida, S. Watanabe,

- and K. Kindo, Phys. Rev. Lett. **101**, 207201 (2008).
- [18] J. Cai, W. G. Macready, and A. Roy, arXiv preprint arXiv:1406.2741 (2014).
- [19] T. Albash and D. A. Lidar, Phys. Rev. X **8**, 031016 (2018).
- [20] R. Moessner, S. L. Sondhi, and P. Chandra, Phys. Rev. B **64**, 144416 (2001).
- [21] Q. Faure, S. Takayoshi, S. Petit, V. Simonet, S. Raymond, L.-P. Regnault, M. Boehm, J. S. White, M. Månsson, C. Rüegg, P. Lejay, B. Canals, T. Lorenz, S. C. Furuya, T. Giamarchi, and B. Grenier, Nat. Phys. **14**, 716 (2018).
- [22] K. Ghosh, arXiv preprint arXiv:2511.06403 [cond-mat.dis-nn] (2025).

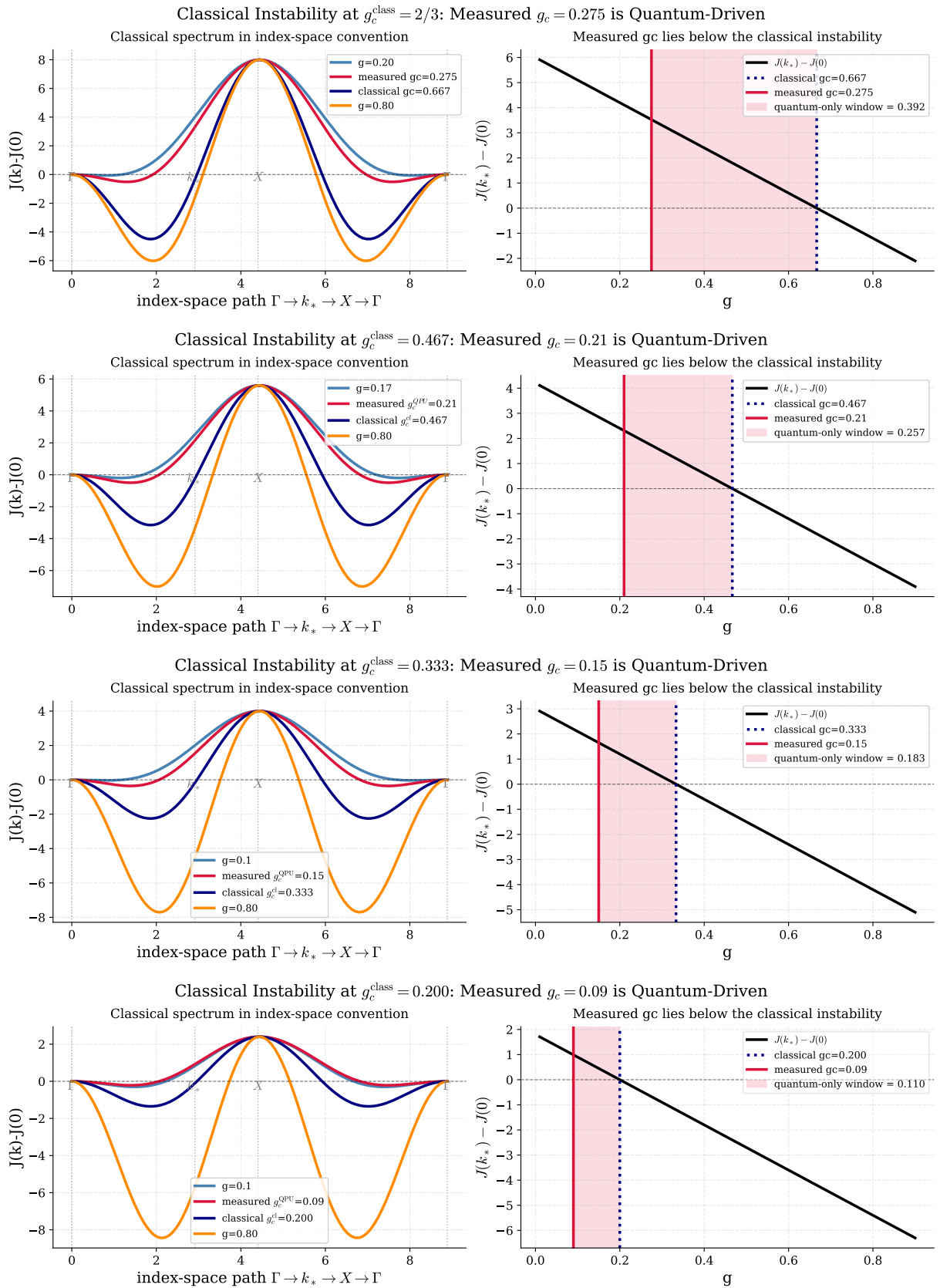


FIG. 1. **Classical spinwave spectra and quantum-only windows.** Each row shows  $J(\mathbf{k}) - J(\mathbf{0})$  along  $\Gamma \rightarrow K \rightarrow X \rightarrow \Gamma$  (left) and the instability diagnostic  $J(\mathbf{k}_*) - J(\mathbf{0}) = 6\alpha - 9g$  vs  $g$  (right). Top ( $\alpha = 1$ ):  $g_c^{\text{class}} = 2/3$ ,  $\Delta g = 0.381$ . Middle ( $\alpha = 0.7$ ,  $\text{NiNb}_2\text{O}_6$ ):  $g_c^{\text{class}} = 0.467$ ,  $\Delta g = 0.257$ . Third ( $\alpha = 0.5$ ,  $\text{BaCo}_2\text{V}_2\text{O}_8$ ):  $g_c^{\text{class}} = 1/3$ ,  $\Delta g = 0.177$ . Bottom ( $\alpha = 0.3$ ,  $\text{FeNb}_2\text{O}_6$ ):  $g_c^{\text{class}} = 0.200$ ,  $\Delta g = 0.107$ . In all four cases the measured  $g_c^{\text{QPU}}$  (solid vertical line) lies within the classically stable FM regime, demonstrating that the transitions are quantum-driven.

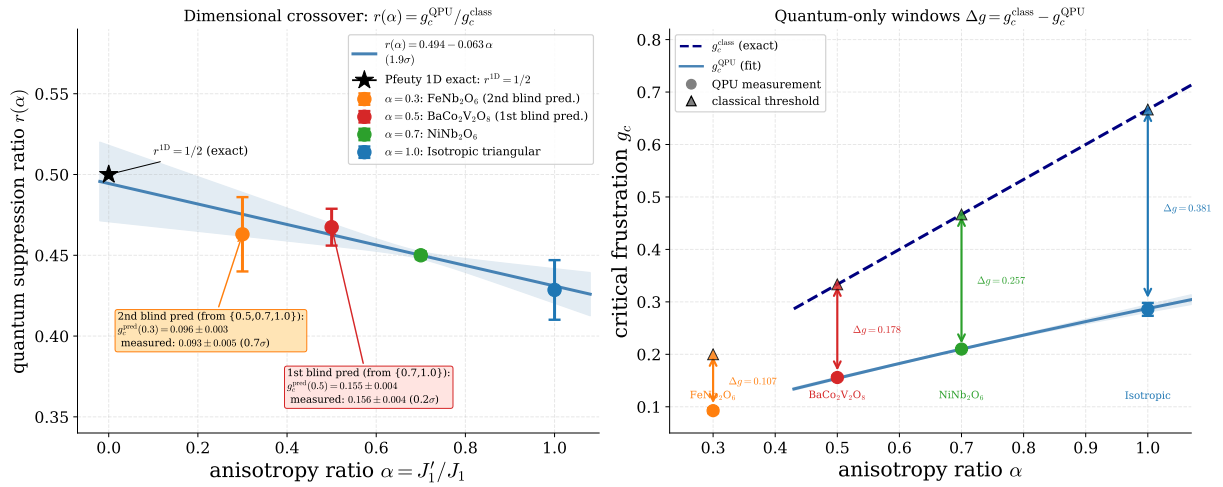


FIG. 2. **Dimensional crossover of the quantum suppression ratio.** *Left:*  $r(\alpha) = g_c^{\text{QPU}}(\alpha)/g_c^{\text{class}}(\alpha)$  vs lattice anisotropy  $\alpha = J'_1/J_1$ . Filled circles: QPU measurements; error bars from  $g_c^{\text{QPU}}$  uncertainties. Solid line: weighted linear fit  $r(\alpha) = 0.494 - 0.063\alpha$  ( $1.9\sigma$ ); shaded band:  $\pm 1\sigma$ . Horizontal dashed line: universal plateau  $\bar{r} = 0.450 \pm 0.002$  ( $\chi^2/\text{dof} = 1.10$ ) confirmed across three quasi-1D geometries. Vertical dotted line: empirical crossover scale  $\alpha^* \approx 0.7$ . Open circle at  $\alpha = 1$ : best estimate from inner Binder pairs ( $r \approx 0.412$ ,  $2.5\sigma$  below plateau); filled circle: conservative weighted mean ( $r = 0.428 \pm 0.018$ ). Filled star at  $\alpha = 0$ : exact 1D TFIM critical point ( $r^{\text{1D}} = 1/2$ , Pfeuty [8]), consistent with the  $\alpha \rightarrow 0$  extrapolation within 1.7 standard deviations. Boxed points: blind predictions confirmed at 0.2 and 0.7 standard deviations (red:  $\alpha = 0.5$ ; orange:  $\alpha = 0.3$ ). *Right:* quantum-only windows  $\Delta g(\alpha) = g_c^{\text{class}}(\alpha) - g_c^{\text{QPU}}(\alpha)$ . Solid curve: Eq. (9). Dashed curve:  $g_c^{\text{class}}(\alpha) = 2\alpha/3$ . The ratio  $\Delta g/g_c^{\text{class}} = 1 - r(\alpha)$  increases as  $\alpha$  decreases, quantifying the growing role of quantum fluctuations as the lattice becomes quasi-one-dimensional.

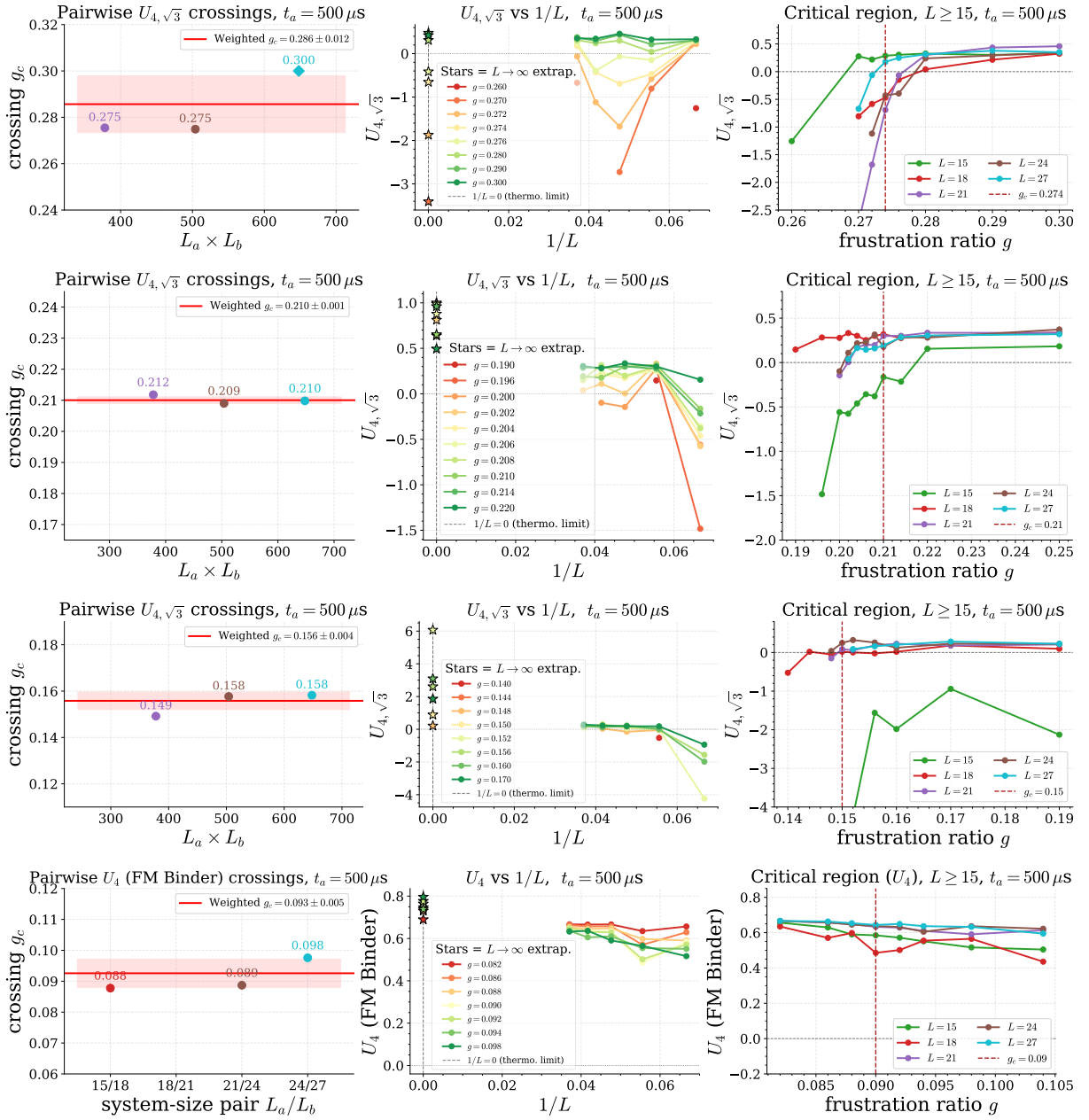


FIG. 3. **Three independent estimates of  $g_c$  at  $t_a = 500 \mu\text{s}$ .** Each row: (left) pairwise  $U_{4, \sqrt{3}}$  crossings vs  $L_a \times L_b$ ; (centre)  $U_{4, \sqrt{3}}$  vs  $1/L$  with  $L \rightarrow \infty$  extrapolation; (right) zoom of the critical region. Top ( $\alpha = 1.0$ ): inner pairs (18, 21) and (21, 24) both cross at  $g \approx 0.275$ ; outer (24, 27) pair crosses at  $0.300$  due to non-monotonic finite-size drift; weighted mean  $g_c^{\text{QPU}} = 0.286 \pm 0.012$ . Middle ( $\alpha = 0.7$ ): three inner pairs span  $\delta g_c = 0.003$ ; weighted mean  $0.210 \pm 0.001$ . Third ( $\alpha = 0.5$ ): inner-pair crossing at  $0.156$ ; sign change between  $g = 0.154$  and  $0.158$ . Bottom ( $\alpha = 0.3$ ): pairwise  $U_4$  crossings give weighted mean  $0.093 \pm 0.005$ ;  $\chi_{\text{FM}}$ -peak extrapolation  $0.095$ – $0.098$ . All three methods agree within  $\pm 0.006$  for  $\alpha \geq 0.5$  and  $\pm 0.008$  for  $\alpha = 0.3$ .

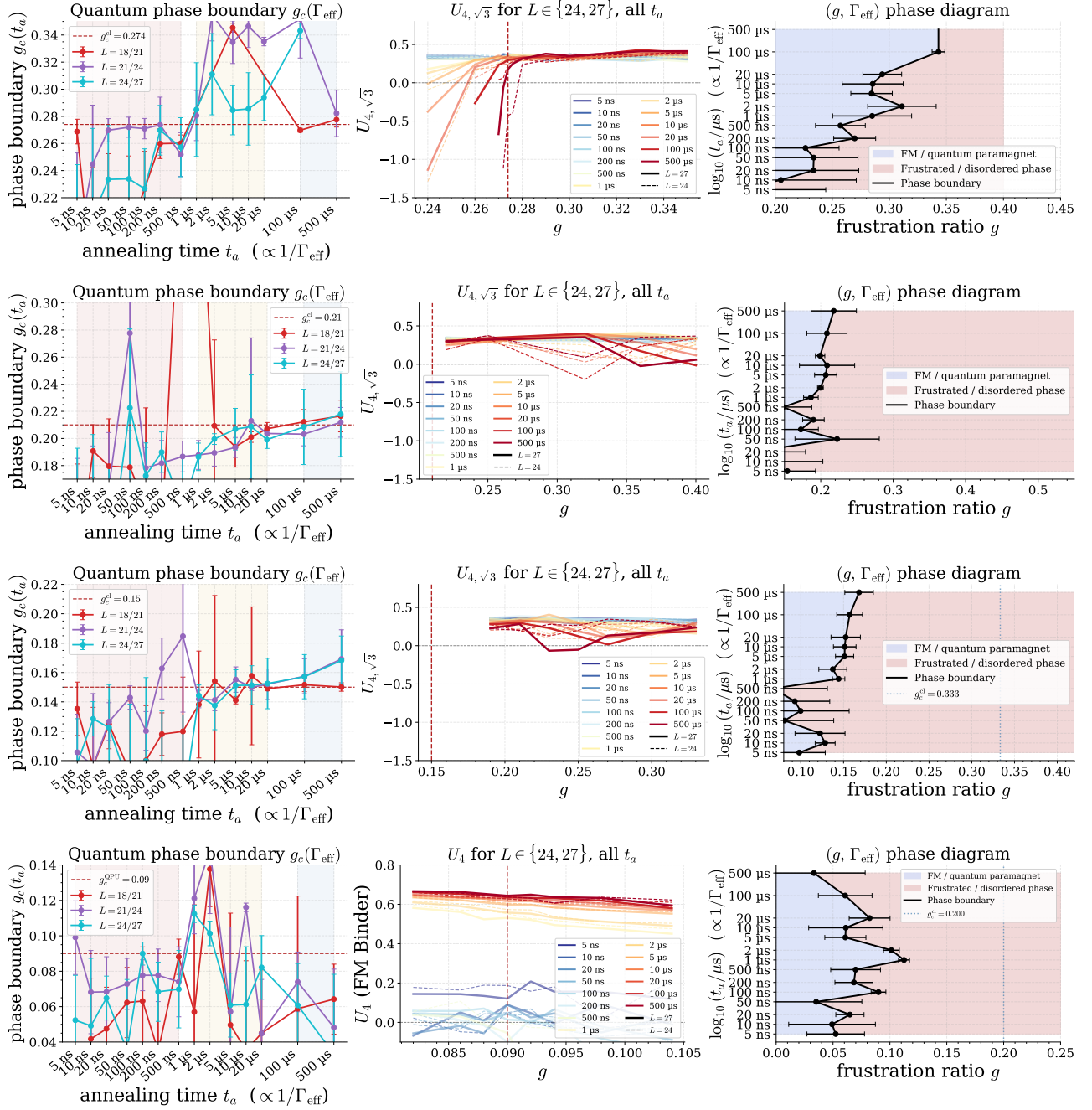


FIG. 4. **Quantum phase boundary**  $g_c^{\text{QPU}}(t_a)$ . Each row: (left) pairwise Binder cumulant crossings vs annealing time  $t_a \propto 1/\Gamma_{\text{eff}}$  ( $U_{4,\sqrt{3}}$  for  $\alpha \geq 0.5$ ;  $U_4$  for  $\alpha = 0.3$ ); (centre) Binder cumulant for  $L \in \{24, 27\}$  across all 14  $t_a$  values; (right)  $(g, \Gamma_{\text{eff}})$  phase diagram. In all four geometries  $g_c^{\text{QPU}}(t_a)$  converges to a  $t_a$ -independent value for  $t_a \gtrsim 20 \mu\text{s}$ , confirming the critical points are intrinsic to the model Hamiltonian and not artefacts of the annealing protocol. Top:  $\Delta g = 0.381$ . Middle:  $\Delta g = 0.257$ . Third:  $\Delta g = 0.177$ . Bottom ( $\alpha = 0.3$ ):  $\Delta g = 0.107$ . The ratio  $\Delta g/g_c^{\text{class}} = 1 - r(\alpha)$  increases with decreasing  $\alpha$ , confirming the dimensional crossover.

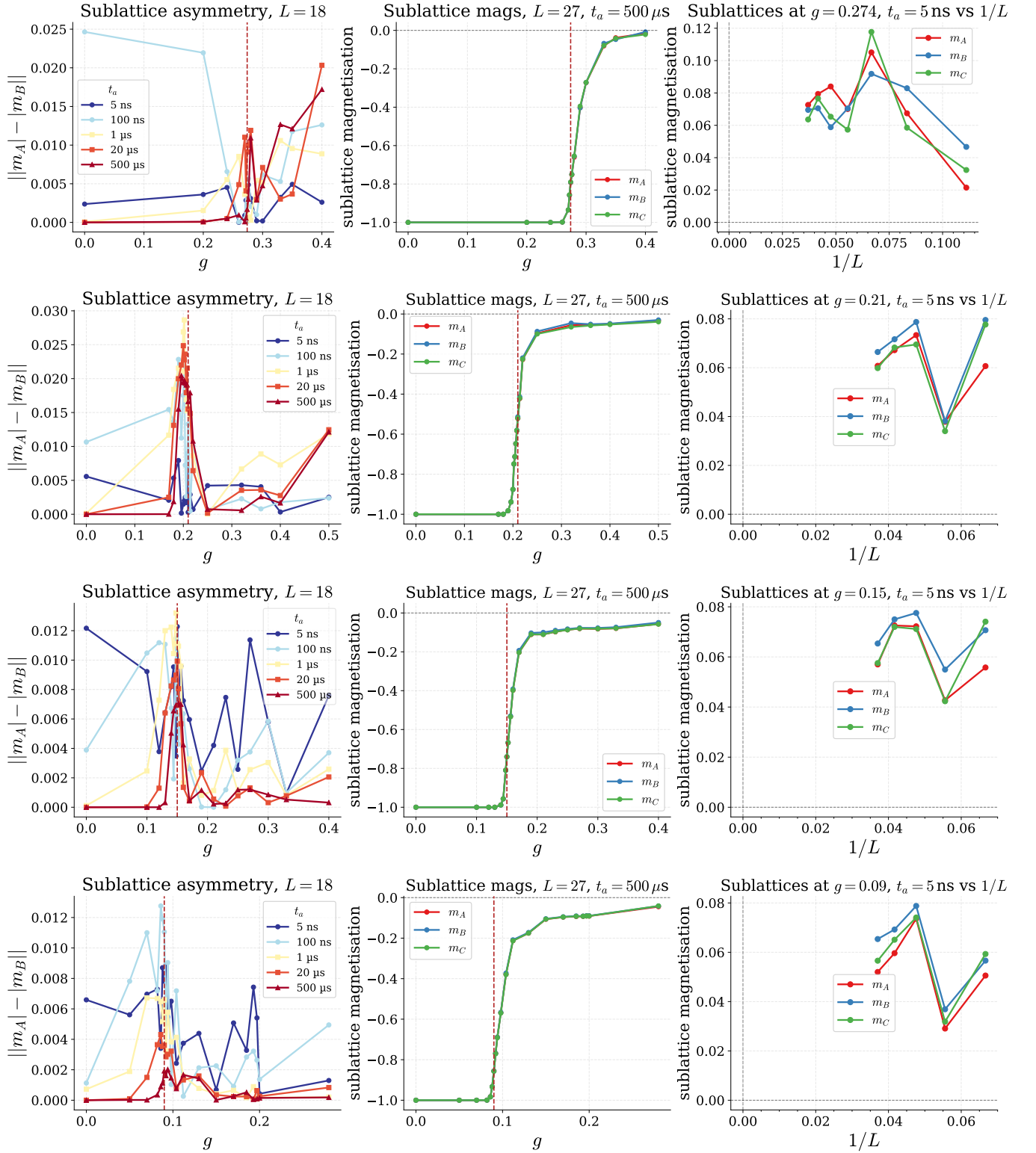


FIG. 5. **Direct FM-to-paramagnet transition across all four geometries.** Each row: (left) sublattice asymmetry  $\|m_A| - |m_B|\|$  vs  $g$  at  $L = 18$ , confirming three-sublattice symmetry throughout; (centre) sublattice magnetisations  $m_A$ ,  $m_B$ ,  $m_C$  vs  $g$  at  $L = 27$ ,  $t_a = 500 \mu\text{s}$ , all three vanishing simultaneously at  $g_c^{\text{QPU}}(\alpha)$ ; (right) sublattice magnetisations vs  $1/L$  at  $g = g_c^{\text{QPU}}(\alpha)$ ,  $t_a = 5 \text{ ns}$ , consistent with zero in the thermodynamic limit. No relative sublattice splitting at any  $g$  or  $t_a$  rules out an intermediate  $\sqrt{3} \times \sqrt{3}$  phase. Top:  $\alpha = 1.0$ . Second:  $\alpha = 0.7$ . Third:  $\alpha = 0.5$ . Bottom:  $\alpha = 0.3$ .

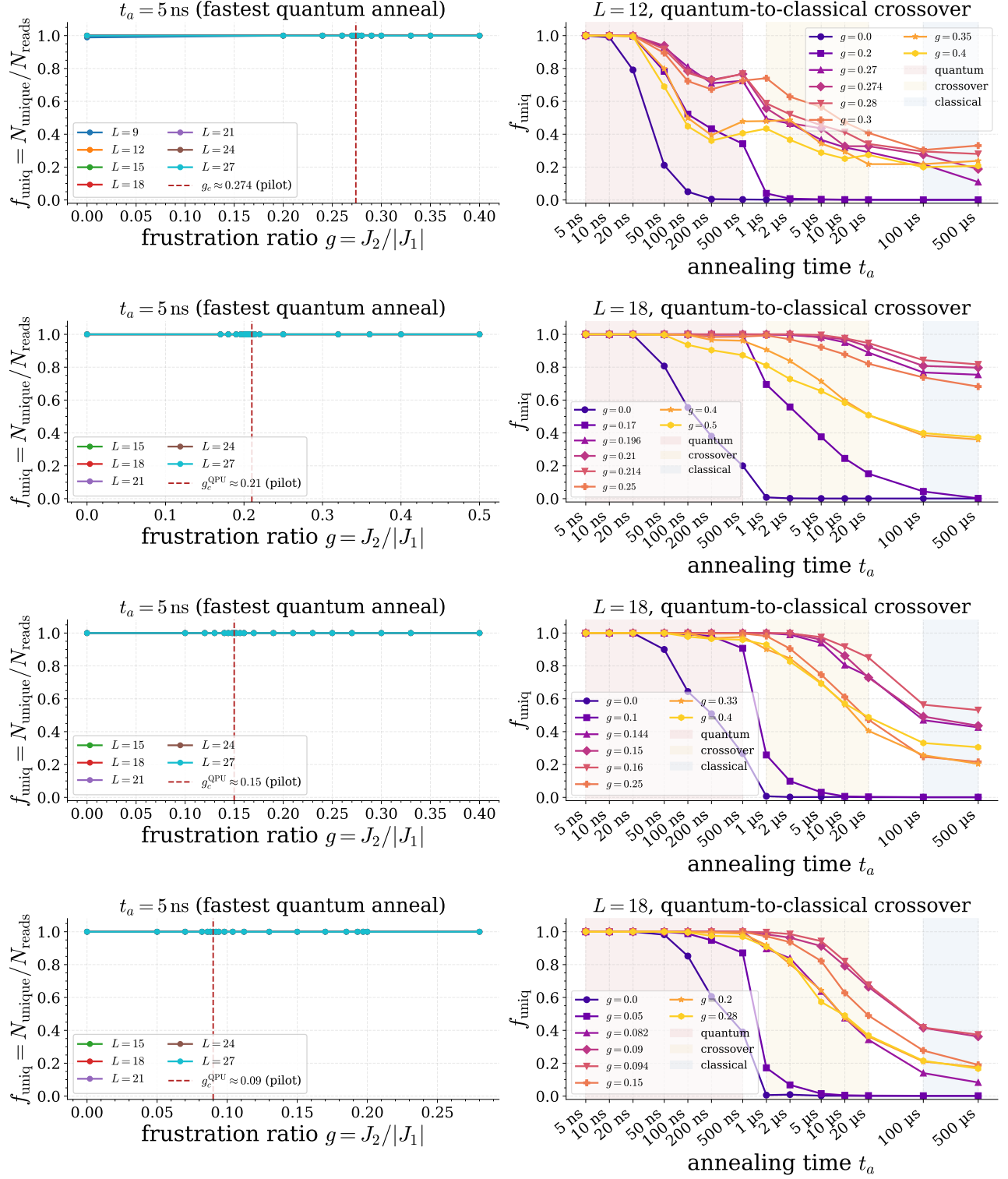


FIG. 6. **Quantum ergodicity bypass and quantum-to-classical crossover.** *Left:*  $f_{\text{uniq}} = N_{\text{unique}}/N_{\text{reads}}$  vs  $g$  at  $t_a = 5$  ns.  $f_{\text{uniq}} = 1.000$  for all  $L$  and all  $\alpha$ : every anneal yields a distinct spin configuration, demonstrating complete ergodicity bypass via quantum tunnelling near each critical point. *Right:*  $f_{\text{uniq}}$  vs  $t_a$  for selected  $g$  ( $L = 12$  for  $\alpha = 1.0$ ;  $L = 18$  for  $\alpha \in \{0.3, 0.5, 0.7\}$ ). The critical point  $g \approx g_c^{\text{QPU}}(\alpha)$  maintains  $f_{\text{uniq}} > 0.5$  until  $t_a \approx 5 \mu\text{s}$ , decaying more slowly than the FM anchor ( $g = 0$ , frozen by  $t_a \approx 1 \mu\text{s}$ ), reflecting enhanced degeneracy at the quantum critical point. Top:  $\alpha = 1.0$ . Second:  $\alpha = 0.7$ . Third:  $\alpha = 0.5$ . Bottom:  $\alpha = 0.3$ .